Graphene-Based Femtogram-Level Sensitive Molecularly Imprinted Polymer of SARS-CoV-2

Seyyed Alireza Hashemi, Sonia Bahrani, Seyyed Mojtaba Mousavi, Navid Omidifar,* Nader Ghaleh Golab Behbahan, Mohammad Arjmand,* Seeram Ramakrishna,* Kamran Bagheri Lankarani, Mohsen Moghadami, and Mohammad Firoozsani

Rapid distribution of viral-induced diseases and weaknesses of common diagnostic platforms for accurate and sensitive identification of infected people raises an urgent demand for the design and fabrication of biosensors capable of early detection of viral biomarkers with high specificity. Accordingly, molecularly imprinted polymers (MIPs) as artificial antibodies prove to be an ideal preliminary detection platform for specific identification of target templates, with superior sensitivity and detection limit (DL). MIPs detect the target template with the "lock and key" mechanism, the same as natural monoclonal antibodies, and present ideal stability at ambient temperature, which improves their practicality for real applications. Herein, a 2D MIP platform consisting of decorated graphene oxide with the interconnected complex of polypyrrole-boronic acid is developed that can detect the trace of severe acute respiratory syndrome coronavirus 2 (SARS-CoV-2) antigen in aquatic biological samples with ultrahigh sensitivity/specificity with DL of 0.326 and 11.32 fg mL^{-1} using voltammetric and amperometric assays, respectively. Additionally, the developed MIP shows remarkable stability, selectivity, and accuracy toward detecting the target template, which paves the way for developing ultraspecific and prompt screening diagnostic configurations capable of detecting the antigen in 1 min or 20 s using voltammetric or amperometric techniques.

1. Introduction

Virus-induced illnesses have become a worldwide health problem that leads to a significantly high death toll each year, highlighting the requirement for advanced detection techniques to monitor and treat the infected people.[1] The outbreak of severe acute respiratory syndrome coronavirus 2 (SARS-CoV-2) could be mentioned as a severe viral outbreak that caused serious threats for humanity through its prompt person-to-person transfer, which cannot be efficiently controlled via traditional detection or treatment techniques.[2] Accordingly, timely detection of pathogenic viruses has become an urgent requirement for healthcare authorities to stop fast transferable viruses through wise isolation strategies. So far, diverse kinds of protocols have been developed to trace viruses in biological samples, among which RT-PCR,[3] cell culture,[4] optical biosensors,[5] electrochemical-based

S. A. Hashemi, M. Arjmand
Nanomaterials and Polymer Nanocomposites Laboratory
School of Engineering
University of British Columbia
Kelowna, BC V1V 1V7, Canada
E-mail: mohammad.arjmand@ubc.ca

S. Bahrani, K. B. Lankarani, M. Moghadami
Health Policy Research Center
Health Institute
Shiraz University of Medical Sciences
Shiraz 71348-45794, Iran

S. M. Mousavi
Department of Chemical Engineering
National Taiwan University of Science and Technology
Taipei City 310635, Taiwan

N. Omidifar
Clinical Education Research Center
Shiraz University of Medical Sciences
Shiraz 71348-14336, Iran
E-mail: omidifarn@sums.ac.ir

N. Omidifar
Department of Pathology
School of Medicine
Shiraz University of Medical Sciences
Shiraz 71348-14336, Iran

N. G. G. Behbahan
Department of Poultry Disease
Razi Vaccine and Serum Research Institute
Shiraz Branch
Agricultural Research, Education and Extension Organization (AREEO)
Shiraz 7188843568, Iran

S. Ramakrishna
Department of Mechanical Engineering
Center for Nanofibers and Nanotechnology
National University of Singapore
Singapore 117576, Singapore
E-mail: seeram@nus.edu.sg

M. Firoozsani
Member of Board of Trustees
Zand Institute of Higher Education
Shiraz 7188773489, Iran

biosensors,[6] piezoelectric biosensors,[7] and ELISA[8] can be mentioned. However, most of these platforms suffer from serious demerits that adversely affect their performances in real applications, necessitating wise strategies to solve their drawbacks. Common diagnostic approaches such as microscopy, cell culture, ELISA, and RT-PCR assays rely on laboratory-based tests that are time-consuming, expensive, and requiring expert personnel. In this matter, RT-PCR shows a high false-negative rate, and ELISA requires a rise in the level of antibodies within the blood that removes the possibility of detecting the infected people at the early stages of their illness.[9] Hence, a low-cost preliminary diagnostic kit is required for reliable and prompt detection of target pathogens or infected people.[10,11]

Specific and selective biosensors are ideal candidates for the rapid identification of pathogenic viruses, chiefly due to their timely detection of infectious illnesses. Such sensors are perfectly beautified with a set of exciting features, including rapid response, excellent sensitivity/specificity, and perfect selectivity toward detecting target pathogens. To address the urgent demand of healthcare authorities for a reliable and preliminary prompt detection approach, molecularly imprinted polymers (MIP) proved to be an ideal alternative over common detection approaches due to their superior specifications such as ease of fabrication, low production cost, high stability, and perfect selectivity/affinity toward template molecules.[12] MIPs are known as artificial antibodies that possess ultraspecific molecular recognition or binding capabilities toward target templates via the creation of noncovalent detection cavities similar to the size and active groups of the target template, which acts as "lock and key." Furthermore, removing the biological template from the polymeric structure of MIPs provides accessible cavities with a memory of the template that saves both morphological and functional features of the template.[13] Such unique shape-memory features of MIPs allow differentiating diverse molecular systems from each other and specifically detect the target pathogen with high accuracy.[14]

In comparison with naturally induced antibodies, MIPs presenting higher chemical stability and lower costs at industrial scales. Additionally, naturally induced antibodies with an ideal affinity toward target pathogens possessing poor stability/durability at high temperatures and pressures. Besides, they cannot tolerate organic solvents or buffers with high or low pH values.[12] Contrary, MIPs exhibit superior reusability and robustness due to their specific functional cavities being highly resilient to environmental factors such as pH, pressure, and temperature.[15] Owing to the specific binding of MIPs with target templates, they have been extensively used for various applications, including purification/separation of target compounds,[16] sensing,[17] intelligent drug delivery,[18] enzyme mimics,[19] antibody mimic,[20] extraction of solid compounds,[21] biomarker,[22] enantioselective,[23] hormone detoxification,[24] drug analysis,[25] food safety,[26] and food/environmental analysis.[27] Correspondingly, the imprinting of the viral antigen has absorbed considerable attention toward itself owing to its excellent potentials for selective virus detection, which is a potential pro for clinical diagnostics, even for *in-vivo* therapy.[28] Furthermore, most MIPs have been fabricated based on the whole virus antigen[29] or a short amino acid sequence of viral protein, i.e., epitope,[30] to develop virus-selective MIPs for recognizing target templates.

In addition, MIPs could be synthesized via diverse combinations of monomer, initiator, cross-linker, and solvents. The MIP's output quality depends on the mixing ratio of monomer to cross-linker, governing interaction mechanisms, and experimental conditions.[12] Electrically conductive polymeric structures such as polyaniline, polypyrrole, polythiophene, and polyacetylene have been widely used to develop MIPs.[31] The polymerization process of the above-mentioned polymers can be conducted at room temperature (RT) within aqueous solutions or organic solvents. Such ideal flexibility in the synthesis of MIPs provides a tremendous advantage for imprinting biomolecules because conformational changes and denaturation can be prevented.[32] Among the potential polymers for developing MIPs, polypyrrole (PPy) is considered as an ideal candidate due to its biocompatibility, high sensitivity, and perfect interaction with template and crosslinker.[31] PPy based MIPs have been used to detect diverse pathogens, including human infected viruses, M13 filamentous bacteriophage, and tobacco mosaic virus.[33]

In addition, graphene and its oxidized forms, i.e., graphene oxide (GO), all of which contain different types of oxygen-based functional groups, viz., carboxyl, epoxy, and hydroxyl, proved to be ideal candidates for biosensing applications because of their excellent chemical, physical, and electrocatalytic properties.[34] Furthermore, the appearance of such hydrophilic functional groups on the surface of GO provides the possibility of decoration and uniform distribution of various types of complexes such as inorganic nanoparticles, metal oxides, semiconductive nanoparticles, noble metals, nanoclusters, quantum dots, and polymeric compounds on the surface of GO flakes that improve their performance for sensor applications.[35,36] What is more, the formed complexes of graphene derivatives with the above-mentioned compounds could facilitate the diffusion rate of diverse biomolecules and improve their biocatalytic activity toward biosensing.[37] In this regard, coupling graphene flakes with metal nanoparticles[35] and polymers[38] could enhance the biocompatibility of the resulting complex, provide the possibility for selective conjugation with the target biomolecules, and improve the active surface area of the developed configuration, making the graphene-based platforms ideal for biosensing applications.[37,39,40]

Additionally, graphene oxide (GO) is considered a highly ideal 2D substrate to improve sensors' active surface area and sensitivity toward detecting target pathogens or chemical compounds.[11,41] GO possesses exciting features such as ease of fabrication, transducer properties, superior activity/reactivity, and the presence of hydrophilic functional groups that provide the possibility for homogeneous distribution of modifiers on its surface.[40,42,43] Moreover, boronic acid-derived compounds, offering superior affinity toward glycoprotein structures, and their consumption as crosslinkers could considerably enhance the sensitivity and selectivity of derived MIPs toward target templates.[44]

Herein, we have developed a highly porous and super active MIP based on the decorated graphene oxide flakes with an interconnected complex of polypyrrole (PPy)-boronic acid that provides the possibility for ultraspecific, selective and sensitive detection of betacoronaviruses, i.e., SARS-CoV-2, whole virus antigens via shape or functional group memory imprinted cavities within the polymeric structure of the final complex.

The as developed MIP acts the same as a natural antibody and provides the possibility of a "key and lock" reaction like natural immunoreceptors. The developed platform is perfectly characterized via diverse analyses to prove the successful imprinting and extraction steps. Next, the MIP is assigned to voltammetric and amperometric assays, and its total performance toward detecting SARS-CoV-2 antigens in biological and non-biological aquatic samples was precisely assessed.

2. Results and Discussion

2.1. Characterization of Developed Compounds

In this section, all developed NIP or MIP configurations were precisely assessed via diverse analyses to justify their successful synthesis. In **Figure 1**a, a view of the production route of MIPs can be seen. As shown, in phase I, ultrapure graphite
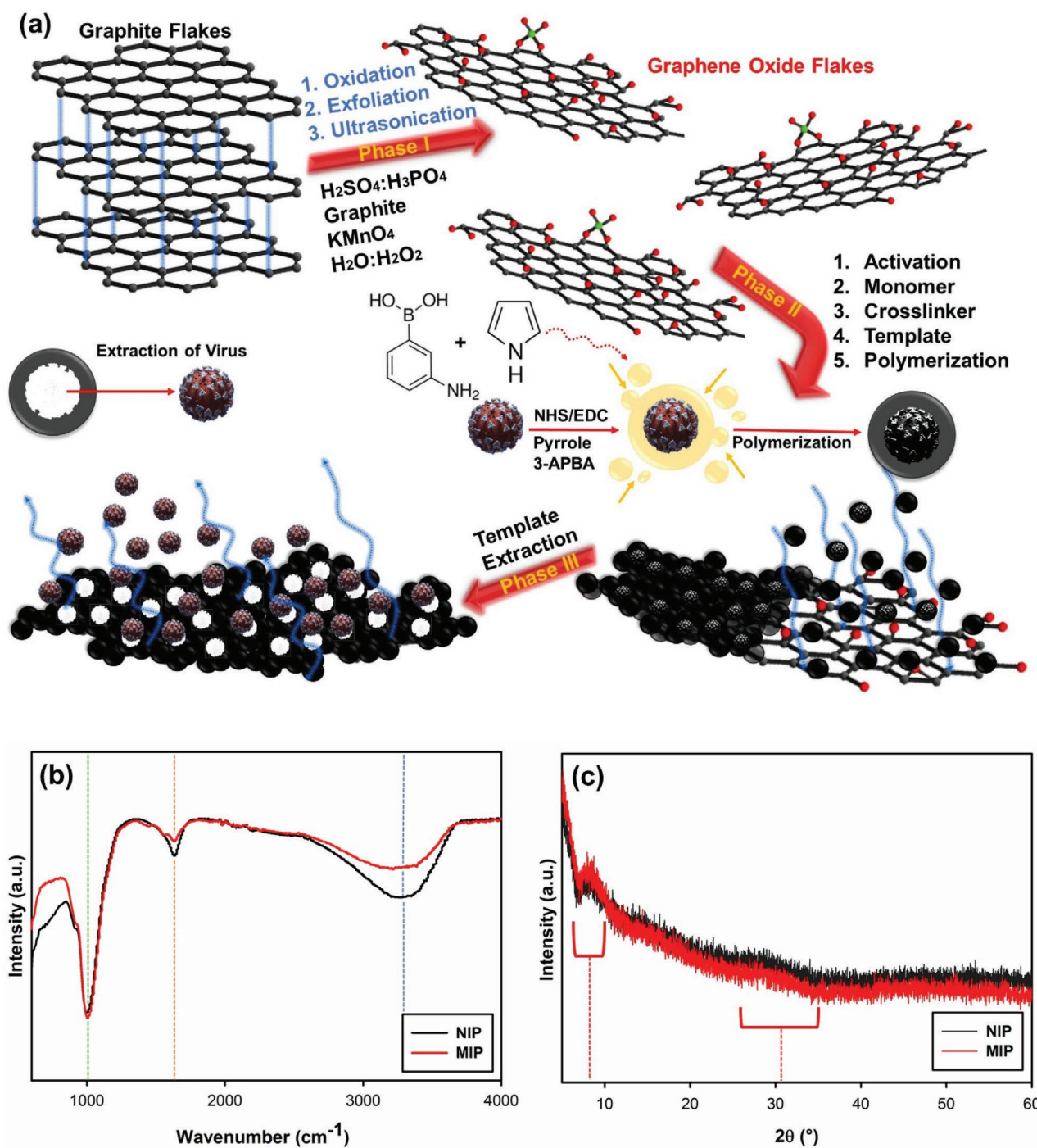

Figure 1. a) Production procedure of MIP platform, b) FTIR spectrums of NIP and MIP, and c) X-ray diffractograms of NIP and MIP.

flakes were oxidated, exfoliated, and further ultrasonicated in the acidic suspension in the presence of oxidation compounds to form well-exfoliated single-layer GO with active functional groups for proper interaction with the imprinted polymeric platform. Accordingly, the GO flakes improve the active surface area, sensitivity, and electroactivity of the developed platform and improve the overall amount of available imprinted cavities on the surface of the final configuration due to their 2D planar structures.

In phase II, the hydrogen-based functional groups and carbonyl groups of the GO were activated via the NHS/EDC complex, followed by the addition of crosslinker (3-APBA), monomer (pyrrole), and template (pure whole virus antigen of SARS-CoV-2 with a concentration of $10^{9.4}$ TCID50 (0.002135 µg mL^{-1})) to the suspension. In this stage, 3-APBA attaches to the template's active functional groups and provides a high affinity toward detecting the template after its extraction. Next, the suspension was mixed to become entirely homogenous, and then the surrounded templates with the crosslinker and monomer were attached on the surface of activated GO flakes. The polymerization occurred via the dropwise addition of the oxidation agent, viz., FeCl$_3$.6H$_2$O, thereby forming an imprinted polymeric structure with a trapped viral template inside it.

In phase III, the template was extracted from imprinted polymers via 10 vol% acetic acid, acetone, and ethanol. Then, the powder was dried and grounded to be prepared for electrochemical assessments. This process leads to forming specific shape memory cavities inside the MIP that save both size and functional groups of the template and act according to the "lock and key" mechanism, the same as a natural monoclonal IgG antibody.

Figure 1b,c exhibits the FTIR and XRD spectrums of NIP and MIP complexes. Both NIP and MIP show the same functional groups and 2φ peaks that confirm the successful formation of the as-developed polymeric platforms. As illustrated in Figure 1a, non-imprinted polymer shows three well-defined sharp peaks at 1003, 1634, and 3286 cm^{-1}, attributed to the in-plane vibration of = C-H functional groups of PPy, C = O functional groups of either graphene or 3-APBA and hydroxyl functional groups (-OH), respectively. Likewise, each appeared peak in the FTIR spectrum of molecularly imprinted polymer corresponds to the vibration of = C-H groups of PPy (1003 cm^{-1}), C-N amide of 3-APBA (1444 cm^{-1}), C = C double bond carbon atoms of either graphene, PPy or 3-APBA (1547 cm^{-1}), C = O functional groups of either graphene or 3-APBA (1629 cm^{-1}) and -OH functional groups (3286 cm^{-1}).[43,45] Thus, the achieved results clearly showed the successful integration of used compounds. Additionally, weak peaks appeared in the FTIR spectrum of MIP that mainly arise from 3-APBA after extraction of template, confirming the chemical shape memory of the MIP and providing information of the imprinted template for possible rebinding.

In Figure 1c, X-ray diffractograms of NIP and MIP configurations can be seen. As demonstrated, both NIP and MIP complexes showed well-defined peaks at 2φ of 8.1 and 28.8, corresponding to the integrated repeated unit of polypyrrole with 3-APBA and graphene oxide flakes. More details of the XRD spectra can be seen in Table S1 in the Supporting Information.

Figure 2a,b shows FESEM images of NIP and MIP complexes, respectively. As depicted in Figure 2a (I-IV), semispherical nanoparticles of an integrated platform of polypyrrole-boronic acid were homogeneously distributed throughout the GO flakes' surface and formed a hybrid platform with 2D morphology and boosted the specific surface area of the final composition. Besides, as shown in part IV, integrated
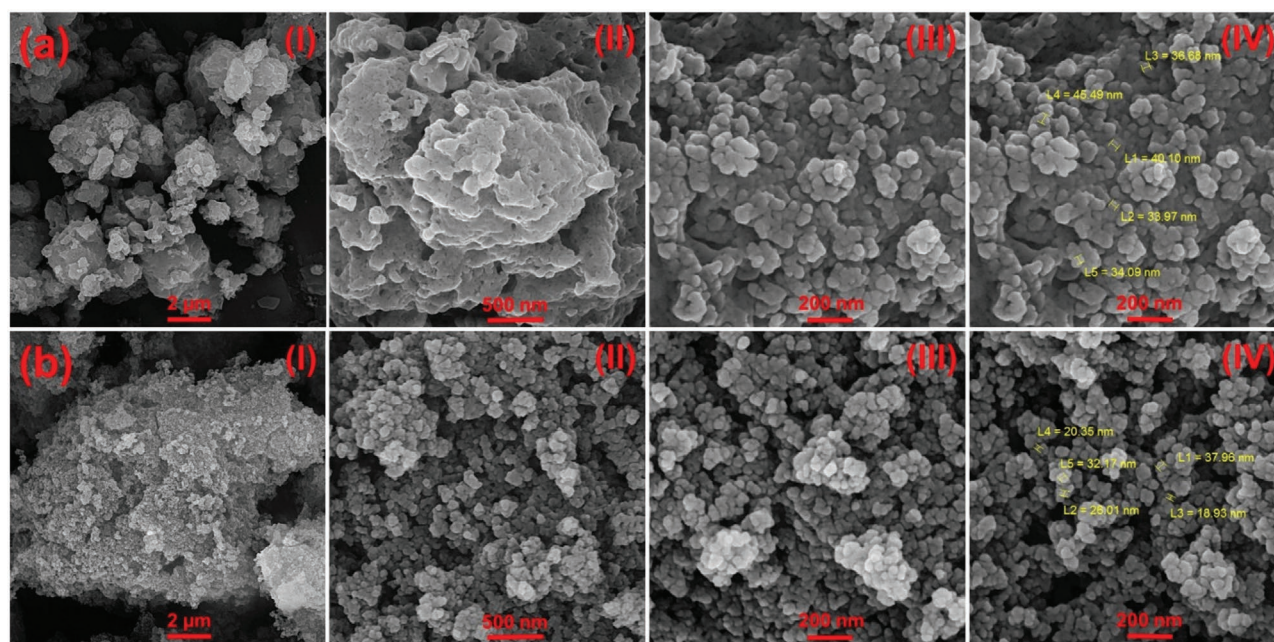

Figure 2. FESEM images of a) NIP and b) MIP at diverse scale bars, viz., I) 2 µm, II) 500 nm, and III,IV) 200 nm; size distribution of each compound can be seen in part (IV).

2101466 (4 of 12)

**ADVANCED
SCIENCE NEWS**
www.advancedsciencenews.com

**ADVANCED
MATERIALS
INTERFACES**
www.advmatinterfaces.de

polypyrrole-boronic nanoparticles, presenting average particle size between the range of 33.97–45.49 nm, provide nanoscale morphology for proper imprinting of the target template. Figure 2b (I-IV) show FESEM images of the SARS-CoV-2 imprinted polymer. The same as NIP, MIP also exhibits a well-defined 2D morphology decorated with integrated polypyrrole-boronic nanoparticles. As depicts in part (IV), the average particle size of the imprinted polymeric platform lies in the range of 18.93–37.96 nm. This outcome shows that integrating the polymeric platform with the target template led to a slight decline in the average size of the imprinted platform that could improve the active surface area of the MIP in interaction with the template.

In **Figure 3**, TEM images of NIP and MIP complexes can be seen. As demonstrated in Figure 3aI–IV, NIP exhibits a well-defined 2D single-layer graphene oxide decorated with integrated polypyrrole-boronic nanoparticles. These data are in well accord with obtained outcomes via FESEM analysis and confirm the homogeneous distribution of integrated polymeric platform on the GO surface, which provides a larger surface area and better interaction toward detection of target templates. Furthermore, as illustrated in Figure 2bI–VI, the MIP is successfully synthesized with the required shape-memory cavities of the template, which provides specific interaction with the target biomolecule. Correspondingly, extraction of the template from the imprinted polymer led to the formation of nano-sized cavities throughout the surface of the decorated GO that eases the interaction of MIP with the template and provides superior specificity toward detection of the target compound owing to the ideal chemical/morphological memory of the generated cavities within the MIP.
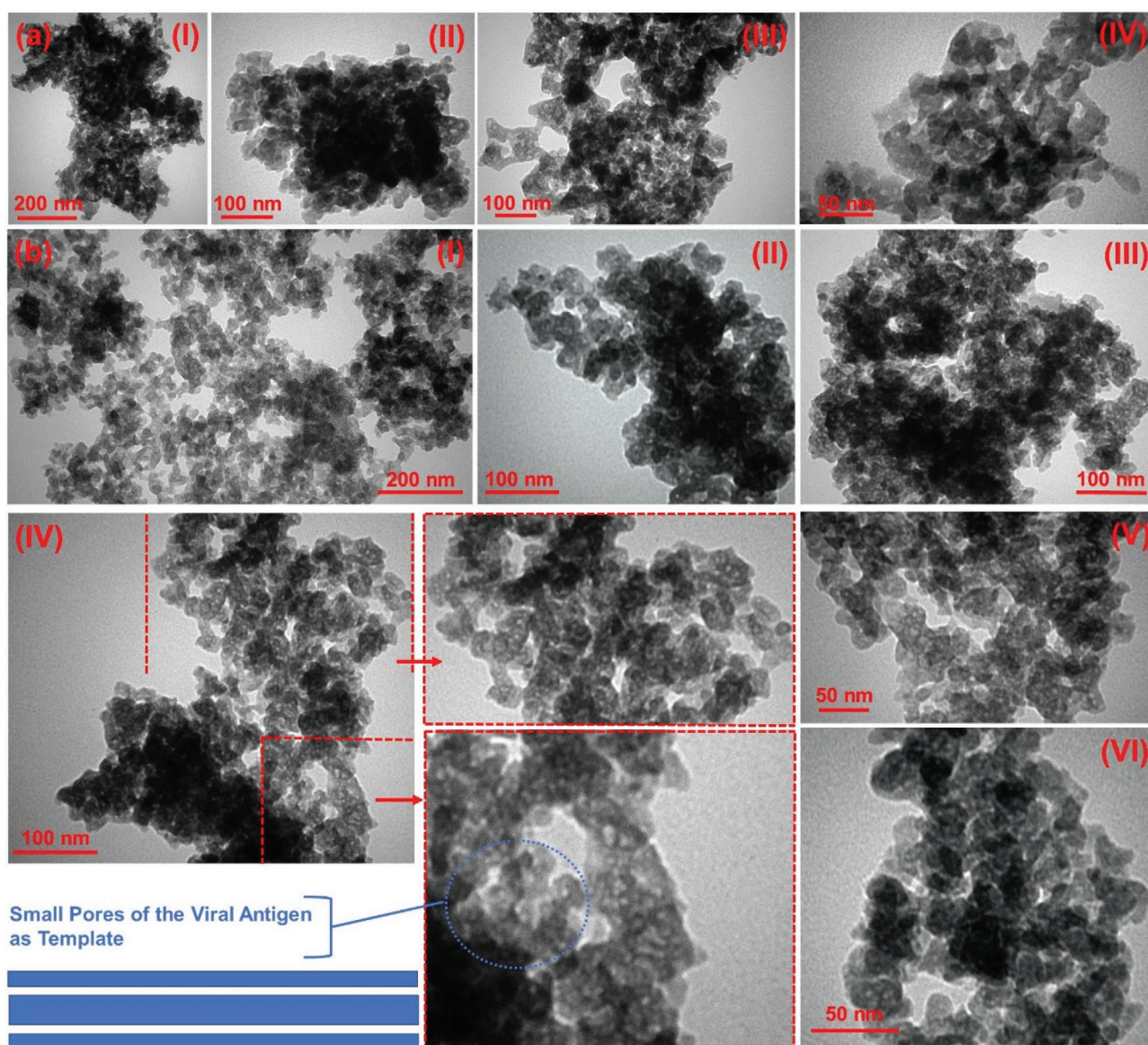

Figure 3. TEM images of a) NIP and b) MIP with different scale bars; in part (b), shape memory imprinted cavities of SARS-CoV-2 within the fabricated MIP can be seen.

**ADVANCED
SCIENCE NEWS**
www.advancedsciencenews.com

**ADVANCED
MATERIALS
INTERFACES**
www.advmatinterfaces.de

Additionally, in Figure S1a,b in the Supporting Information, elemental distribution of NIP and MIP along with their ratios can be seen, respectively. As depicted in Figure S1a in the Supporting Information, NIP consisted of 18.31 A% carbon, 9.82 A% nitrogen, 55.96 A% oxygen, 7.54 A% phosphorus, 0.15 A% sulfur, 1.10 A% potassium, 7.06 A% iron and 0.06 A% boron. Besides, as shown in Figure S1b in the Supporting Information, MIP consisted of 32.57 A% carbon, 9.52 A% nitrogen, 44.99 A% oxygen, 6.02 A% phosphorus, 0.24 A% sulfur, 0.59 A% potassium, 5.77 A% iron and 0.30 A% boron. The elemental distribution map of NIP and MIP is demonstrated within Figures S2 and S3 in the Supporting Information, respectively. Achieved data from performed analyses are in perfect accord with each other and confirm the successful fabrication of developed compounds with essential features and elemental distribution.

More importantly, it is bare bone essential to study the generated imprinted cavities within the MIP to assess the successful formation of the imprinted polymer and extraction of template from the MIP. In **Figure 4**a–d, the outcome of BET analysis for NIP and MIP complexes can be seen. As illustrated in Figure 4a,b, the adsorption/desorption isotherm of NIP and MIP complexes at 77 K shows type IV isotherm related to the meso-macroporous compounds (micropores d<2 nm, mesopores 2 nm<d<50 nm and macropores d>50 nm). These plots vividly show that upon creating specific cavities within the MIP, the adsorption rate and pore volume distribution rate are considerably soared. Figure 4c depicts the corresponding t-plots of NIP and MIP complexes. As demonstrated, the upward deviations within the high-pressure region are due to the capillary condensation in meso-macropores.[46] Figure 4d depicts the pore size distribution rate of NIP and MIP. Both NIP and MIP show meso-macropores, while most cavities lie in the range of mesopores. In this matter, upon extraction of the template from the MIP, the overall rate of mesopores and micropores is considerably soared, corresponding to the formation of shape memory cavities in accord with the size of the SARS-CoV-2 antigen. These created shape memory cavities hold the size and chemical information of the target template, and like a natural monoclonal antibody, they only react with their target antigen through highly specific interactions (Figure 4e).

In **Table 1**, extracted data from the BET analysis can be seen. As demonstrated, the creation of imprinted cavities within the MIP complex led to a 161.93% and 183.18% increase in the specific surface area and total pore volume compared with the non-imprinted complex. These outcomes show the successful formation of specific shape memory cavities within the polymeric structure of MIP as artificial antibodies to detect SARS-CoV-2. More details can be seen in Table 1, which vividly prove the formation of specific cavities within the MIP.

Figure 4f,g shows the 2D and 3D AFM maps of NIP and MIP platforms, respectively, which provide valuable information regarding the imprinted surface cavities on the active surface area of the MIP complex. As depicts in Figure 4f, the NIP complex shows a uniform surface with distributed non-imprinted polymeric nanoparticles of PPy and 3-APBA. The NIP platform shows average roughness (R_a), RMS roughness (R_q), and peak-to-valley roughness (R_t) of 314.4 pm, 479.4 pm, and 4.695 nm, respectively. On the other hand, the MIP complex shows a quite different morphology than NIP due to the creation of imprinted cavities within its polymeric part. As shown in Figure 4f, the MIP complex shows R_a, R_q, and R_t of 865.6 pm, 1.170 nm, and 10.34 nm, respectively. As vividly illuminated within 3D AFM maps, extraction of template from the MIP led to the formation of shape memory cavities that provides the possibility of the specific rebinding with the target template. Correspondingly, an increase in the R_t from 4.695 nm for NIP to 10.34 nm for MIP clearly shows the formation of pores with larger depth in the surface of the MIP generated from the imprinted templates in the polymeric part of the MIP.

2.2. Electrochemical Performance of Molecularly Imprinted Polymer

Impedance and voltammetric techniques were utilized to assess the fabrication steps of the developed NIP and MIP based biosensors in the electroactive probe solution containing 3×10^{-3} M hexacyanoferrate (1:1 molar ratio of $(Fe(CN)_6)^{3-/4-}$), 0.01 M PBS (pH 7.4) and 0.01 M KCl. Therefore, the interfacial characters of the electrode surfaces after each modification step can be effectively tracked by the CV and EIS measurements. In **Figure 5**a–c, a view of CV plots of bare GCE and modified GCE with either NIP or MIP-based compounds with diverse conditions can be seen. As depicts in Figure 5a, a reversible redox behaviour of $(Fe(CN)_6)^{3-/4-}$ was observed at the unmodified GCE, indicating the conducting nature of the bare electrode with current output (I_p) of 11.32 µA. Additionally, as clearly depicted in Figure 5 a,b, NIP modified GCE increased the I_p of the redox probe from 11.32 µA to 26.14 µA, which shows about 130.9% increase in the current output compared with the bare GCE. This outcome illuminates the fact that the decoration of GCE with NIP can significantly boost the current response and sensor sensitivity toward oxidation/reduction of the redox probe. More importantly, upon adding 3 fg mL^{-1} SARS-CoV-2 antigen to the NIP and its subsequent extraction via 10 vol% acetic acid and ethanol, no considerable change in the I_p of the sensor was observed, indicating the absence of shape memory cavities in the structure of NIP. Correspondingly, adding the same amount of antigen to the NIP suspension did not affect the I_p of the redox probe. Of note, NIP after addition and extraction of the antigen and rebinding with the antigen, show similar CV patterns with nearly the same I_p values. These outcomes show that the imprinted cavities could decline the NIP's sensitivity toward identifying the whole virus antigen of SARS-CoV-2.

On the other hand, as depicted in Figure 5a,c, the MIP showed remarkable performance toward detecting SARS-CoV-2 in the redox probe. In this matter, decoration of GCE with the MIP-based sensor after extraction of antigen increased the I_p of the redox probe by about 571.64%, showing the remarkable electrocatalytic performance of the sensor toward detection of target pathogens. Interestingly, both sensors based on the MIP before extracting antigen and MIP after rebinding with the antigen showed nearly the same I_p, indicating the specific interaction of MIP with the target template.

The remarkable response of the MIP toward antigen of the SARS-CoV-2 suggests that vacant imprinted sites of SARS-CoV-2 antigen in the polymeric structure of MIP have been occupied with the target antigen, which leads to the creation
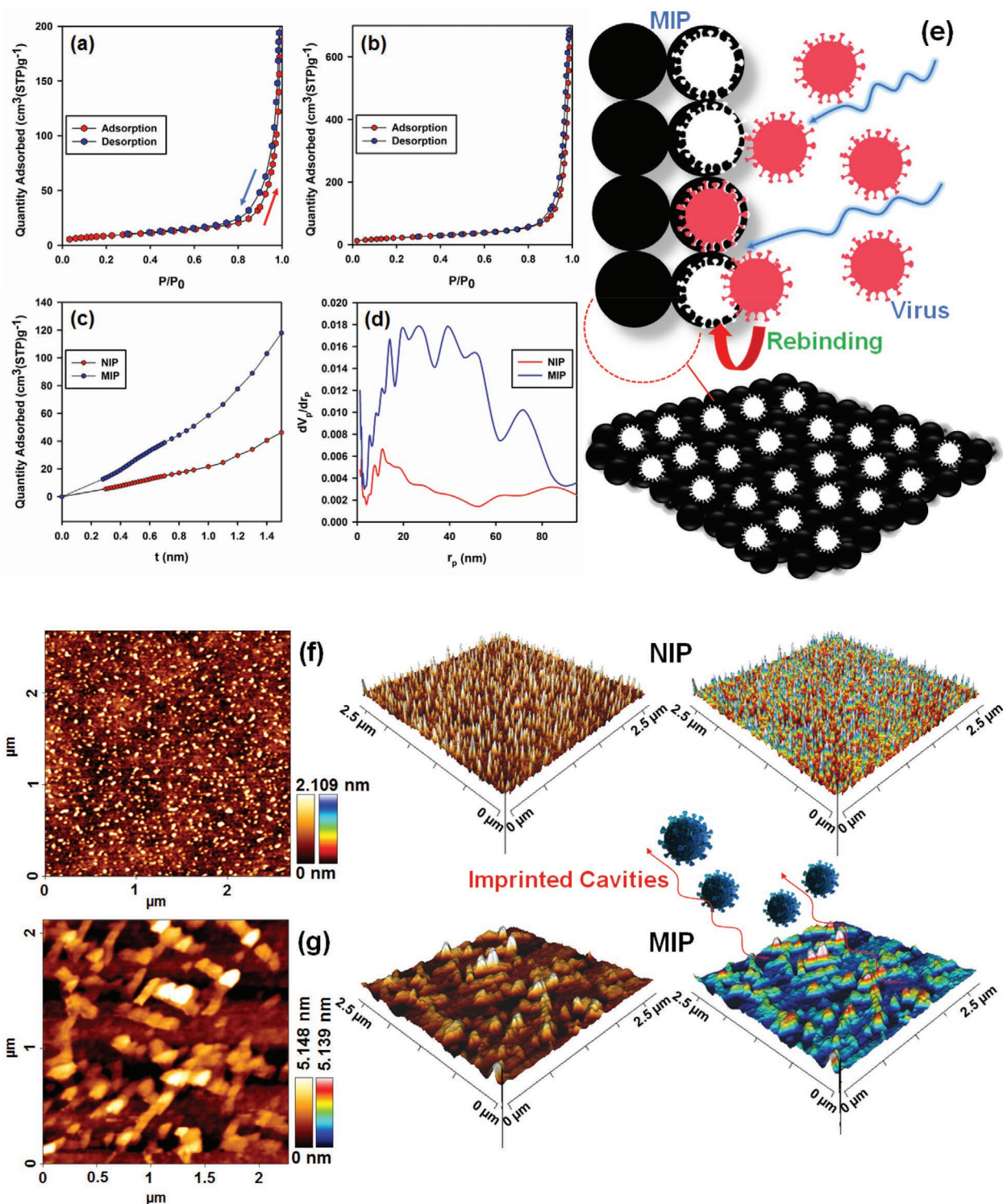
ADVANCED
SCIENCE NEWS

www.advancedsciencenews.com

ADVANCED
MATERIALS
INTERFACES

www.advmatinterfaces.de

Figure 4. a) The nitrogen adsorption/desorption isotherm at 77 K related to the non-imprinted polymer, b) the nitrogen adsorption/desorption isotherm at 77 K related to the molecularly imprinted polymer, c) *t*-plots of NIP and MIP complexes, d) pore size distribution plots of NIP and MIP complexes obtained from the adsorption isotherm of the BET analysis, e) a view of the rebinding process of the molecularly imprinted polymer as an artificial antibody with the viral template; AFM analysis of f) NIP and g) MIP after generation of imprinted specific cavities.

of specific responses in the reaction of MIP with the template. After exposing the electrode to a solution containing SARS-CoV-2 antigen, the current response of the CV assay was

decreased, indicating the specific rebinding of SARS-CoV-2 antigen with the coated MIP on the surface of GCE. Simultaneously, the NIP compound did not show any apparent changes

**ADVANCED
SCIENCE NEWS**
www.advancedsciencenews.com

**ADVANCED
MATERIALS
INTERFACES**
www.advmatinterfaces.de

Table 1. Extracted data from BET analysis for NIP and MIP platforms.

Parameter	Unit	NIP	MIP	Improvement
$a_{s, BET}$	$m^2 g^{-1}$	31.29	81.959	161.93%
$a_{s, Langmuir}$	$m^2 g^{-1}$	5256.1	7286.9	38.63%
a_p	$m^2 g^{-1}$	33.746	95.563	183.18%
Total pore volume ($p/p_0 = 0.990$)	–	0.2954	1.0638	260.12%
Mean pore diameter	nm	37.762	51.92	37.49%
$r_{p, peak}$ (area) from BJH plot	nm	10.65	39.01	266.29%
$V_{m, BET}$	$cm^3(STP)g^{-1}$	7.1889	18.831	161.94%
$V_{m, Langmuir}$	$cm^3(STP)g^{-1}$	1207.6	1674.2	38.63%
V_p	$cm^3 g^{-1}$	0.2946	1.0651	261.54%

compared with MIP after interaction with the antigen due to the absence of specific sites for interaction with the target antigen. These outcomes clearly show the creation of shape memory cavities in the imprinted polymeric platform that specifically react with the target template.

The EIS analysis was also performed to assess the electrode/electrolyte interface and the ideal performance of NIP and MIP compounds toward detecting SARS-CoV-2 antigen. Figure 5d exhibits the Nyquist plots of the developed electrochemical-based sensors with diverse conditions. Correspondingly, the equivalent Randles circuit, viz., $(R_s(C(R_{ct}W)))$, for the demonstrated Nyquist plots is fitted with the experimental data to obtain valuable electrochemical parameters for each sensor, where R_S, R_{ct}, C_{dl} and Z_w corresponds to the electrolyte resistance, electron-transfer resistance, double-layer capacitance, and Warburg impedance, respectively. Furthermore, the R_{ct} value of the as-prepared sensors at diverse conditions was assessed to

check their surface properties and performances in interaction with the target template. As demonstrated in Figure 5d, each modified GCE configuration showed a different R_{ct} value from its full features and conditions. Likewise, GCE, GCE-NIP, GCE-MIP before extraction, GCE-MIP after extraction, and GCE-MIP after rebinding with the viral template showed R_{ct} values of about 1698 Ω, 1203 Ω, 698 Ω, 353.26 Ω and 372.98 Ω, respectively. From the obtained data, it can be seen that upon the decoration of GCE with MIP, the value of R_{ct} declined compared to the bare GCE, which is due to the higher electron transfer rate and electrical conductivity of the integrated platform of polypyrrole and boronic acid-based compounds. Moreover, the MIP, after rebinding, showed resistivity of 372.98 Ω, indicating remnant of active cavities in the imprinted-polymer for specific interaction with target template till reaching the resistivity of 698 Ω (resistivity of MIP before extraction of the template).

Additionally, when the embedded viral template is eluted out of the imprinted polymeric platform, the diameter of the high-frequency semicircle (R_{ct}) is reduced significantly to about 353.26 Ω, exhibiting a considerable decrease in the resistance of the MIP complex upon extraction of viral antigen from it. This remarkable two-fold decline in the resistance of the MIP complex after extraction of viral antigen could be attributed to the formation of imprinted viral cavities upon removal of the template from the MIP complex. The generated cavities act as channels for the diffusion of $(Fe(CN)_6)^{3-/4-}$ within the coated MIP film on the surface of GCE, which could generate a unique electrochemical pattern with a specific peak for its target template.

Contrary, incubation of MIP with the antigen of SARS-CoV-2 leads to specific rebinding between the MIP and viral template, leading to a considerable soar in the diameter of the
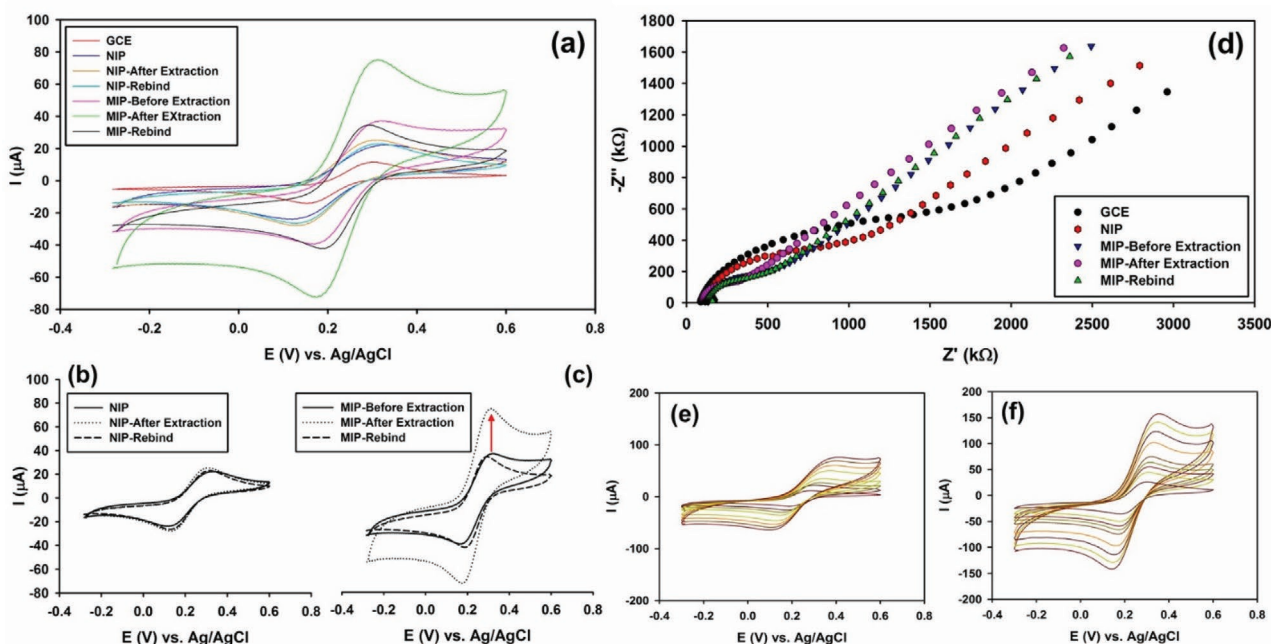

Figure 5. a) CV plots of developed compounds in the probe solution, b) CV plots of NIP complexes at diverse conditions, c) CV plots of MIP complexes at diverse conditions, and d) Nyquist plots of developed platforms in the probe solution; effect of scan rate between the range of 0.01–0.5 V.s^{-1} on the electrochemical response of the e) NIP and f) MIP configurations after extraction of the template in the probe solution.

**ADVANCED
SCIENCE NEWS**

www.advancedsciencenews.com

**ADVANCED
MATERIALS
INTERFACES**

www.advmatinterfaces.de

semi-circle region of the Nyquist plot of the MIP complex after rebinding with the template. This outcome is mainly due to the occupation of the imprinted cavities in the MIP complex and creating a barrier against the arrival of a hexocyannate probe to the electrode surface. It is worth noting that the R_{ct} value of the MIP before extraction of the template was still smaller than the rebonded form, implying that the SARS-CoV-2 antigen occupied only a portion of imprinted cavities. However, the NIP modified GCE exhibited a negligible change in the sensor's resistance even upon interaction with the viral template, highlighting the prominent role of the MIP complex toward specific detection of SARS-CoV-2 antigen in diverse aquatic media.

Besides, surface homogeneity and porosity of the developed compounds are also assessed to check the electrocatalytic performance of the developed nanomaterials toward target templates. The "n" parameter, which indicates surface inhomogeneity close to unity in the ideal smooth electrode surface, is obtained to check the quality of each prepared electrode. The "n" parameter indicates surface inhomogeneity and surface porosity of the as developed MIP-based biosensor. In this matter, GCE, GCE-GO, GCE-NIP, and GCE-MIP showed n parameters of 0.89, 0.84, 0.92, and 0.96, respectively. The modified GCE with MIP complex showed the highest value for the n parameter, which shows this configuration's ideal surface porosity than the NIP or bare GO-GCE due to the generation of specific cavities throughout its polymeric structure.

The effect of the potential scan rate (v) on the electrochemical properties of each NIP or MIP sensor in the range of 0.01–0.5 V.s^{-1} was investigated by CV assay in the probe solution containing 3×10^{-3} M Fe(CN)$_6^{3-/4-}$ (Figure 5e,f). Based on the slope of the I_p-$v^{1/2}$ plot and Randles-Sevcik equation ($I_p = 2.69 \times 10^5$ $n^{3/2}A_{eff}D^{1/2}v^{1/2}C$), the electrochemically active surface area (ECSA) of each electrode configuration was estimated. In the Randles-Sevcik equation, I_p is the peak current (A), n is the number of electrons transferred, A_{eff} is the effective area (cm^2), D is the diffusion coefficient of 3×10^{-3} M K$_3$Fe(CN)$_6$ and 0.01M KCl (cm^2.s^{-1}), v is the scan rate (V.s^{-1}) and C corresponds to the bulk concentration of the redox probe (mol.mL^{-3}). In this matter, GCE, GCE-NIP, and GCE-MIP platforms exhibited A_{eff} of 3.14, 3.32, and 4.14 mm^2, respectively, where GCE-MIP shows 31.84% and 24.69% more porosity compared with the bare GCE and GCE-NIP; these outcomes are in accord with previously obtained data and confirm the creation of specific cavities in the imprinted polymeric platform that led to the soar in the structural porosity of the MIP complex.

The electrochemical performance of the developed NIP and MIP complexes was assessed toward detecting SARS-CoV-2 antigens in aquatic biological or non-biological media via voltammetric assays in the electrolyte, consisting of 0.01 M KCl and 0.01 M PBS at pH 7.4. In addition, control experiments were also carried out with a similar procedure using the coated GCE with the non-imprinted platform, viz., NIP, to check the specific response of the MIP to the target template.

The DPV assay measured the current variation (ΔI) of the oxidation peak before and after exposing the electrodes to a standard stock solution of SARS-CoV-2 antigen. Extracting the current response of both NIP and MIP complexes, including their current variation (ΔI) and diversities in the intensity of current peak upon rebinding with the viral antigen, provides

valuable information regarding the capability of either NIP or MIP toward specific electrochemical detection of SARS-CoV-2 in the target aquatic sample. In Figure S4 in the Supporting Information, the current variation of NIP and MIP-based sensors can be seen, exhibiting a superiorly high current response for the imprinted polymeric platform. Simultaneously, the non-imprinted one shows negligible current variation due to the absence of specific cavities for possible rebinding with the template.

The rationale behind the higher electrochemical response of the imprinted platform is that the imprinting process creates recognition sites for SARS-CoV-2 antigen and improves the specificity of the sensor towards precise detection of target templet in aquatic samples. Furthermore, this sensor's much higher electrochemical response is attributed to the formation of imprinted sites in the MIP complex, which provide ideal pathways for the diffusion of target analyte toward the vacant areas of the MIP, leading to a significant soar in the intensity of the current peak.

Moreover, the considered configuration of the MIP is also playing a crucial role in the sensitive, specific, and accurate detection of viral antigen. In this matter, GO flakes as ideal substrates for the imprinted polymer turning the morphology of the polymeric platform from nearly spherical to 2D broad active flakes with boosted specific surface area. Additionally, the GO provides a high amount of hydrophilic functional groups, increasing the available sites for strong hydrogen bonding and electrostatic/π-π interactions, thereby leading to a highly active MIP complex with boosted performance. Polymerization of the pyrrole monomer on the surface of GO in the presence of a template could create an imprinted polymeric complex with excellent electrical conductivity, ideal water-solubility, and biocompatibility, capable of specific detection of imprinted templates in different samples. More importantly, boronic acid and its derivatives have shown exceptional capability toward reaction with *cis*-diols groups such as glycoproteins and carbohydrate compounds by forming an interconnected complex. Boronic acid with tetrahedral form binds with the *cis*-diols of glycoprotein to form covalent bonds. This matter could be attributed to the N and O atoms offered by the glycoprotein to stabilize the tetrahedral form. 3-APBA provides better interaction with glycoproteins and improves the developed sensor's affinity, specificity, and sensitivity. Such a platform could specifically detect the target template and give the same responses compared with natural monoclonal IgG antibodies.

The analytical performance of SARS-CoV MIP is assessed via recording the peak current in differential pulse voltammetric measurements. The specific binding of the SARS-CoV-2 antigen to the imprinted sites was revealed by increasing the oxidation peak current. A view of obtained data can be seen in **Figure 6**a. To evaluate the sensitivity of the proposed biosensor, the analytical calibration curve was plotted upon recording the current responses of diverse concentrations of SARS-CoV-2 antigen in the electrolyte at optimum conditions via DPV assay (inset of Figure 6a). The peak current is at a minimum value in the absence of a virus. It gradually increases upon soar in the viral load due to the rebinding of viral antigen with cavities of MIP specifically made for the target viral template. As illustrated, the calibration curve showed a good linear relationship
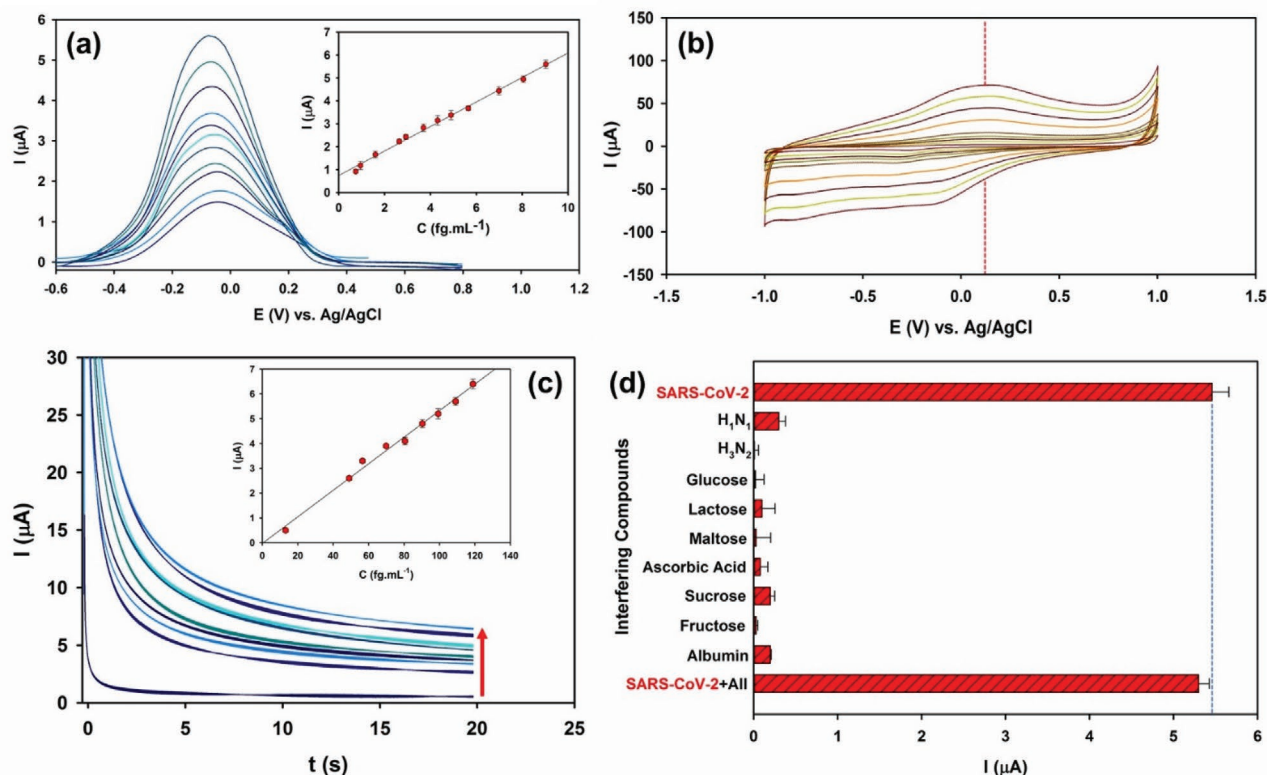
**ADVANCED
SCIENCE NEWS**
www.advancedsciencenews.com

**ADVANCED
MATERIALS
INTERFACES**
www.advmatinterfaces.de

Figure 6. a) DPV pattern of SARS-CoV-2 antigen detection by MIP configuration, insert shows the respective calibration curve; b) effect of scan rate between the range of 0.01–0.5 V.s^{-1} on the electrochemical response of the MIP after interaction with the viral template (insert can be seen in Figure S5 in the Supporting Information), c) rapid (20 s) amperometric response of the MIP toward viral antigen, the insert shows the respective calibration curve of amperometric assay; d) effect of interfering compounds on the current response of the MIP toward detection of SARS-CoV-2 antigen.

between the current response and the respective viral concentration in the range of 0.74–9.03 fg mL^{-1}. The linear relationship could be represented by the equation I_P (µA) = 0.535 (C_{Virus}) (fg mL^{-1}) + 0.74 with a correlation coefficient (R^2) of 0.995. Based on the obtained calibration curve, the MIP complex showed a limit of detection (LOD) and limit of quantification (LOQ) (at a signal-to-noise ratio of 3/10) of 0.326 and 0.658 fg mL^{-1} toward detection of SARS-CoV-2 antigen. Besides, the as-prepared biosensor also exhibited a remarkable sensitivity of 12.935 µA fg mL^{-1} cm^{-2}, which shows the MIP complex's superior sensitivity toward detecting the target antigen. The achieved data vividly illuminate the prominent role of the decorated interconnected polymeric complex of polypyrrole-boronic acid on the surface of GO toward specific/sensitive detection of target glycoprotein templates through a synergistic effect.

The effect of variable scan rate on the kinetics of the modified GCE with MIP configuration was assessed using CV cycles from 0.01 V.s^{-1} to 0.5 V.s^{-1}; a view of obtained data and respective calibration curve can be seen in Figure 6b and Figure S5 (Supporting Information). In this matter, the electrochemical oxidation signal indicates a regular soar in the peak intensity (µA) upon an increase in the scan rate. The shift of obtained peaks toward more positive potential values upon an increase in the CV assay scan rate revealed that the MIP configuration's electrochemical process is chiefly governed via a surface-restrained mechanism. This mechanism is an indicator of the

absorptive process and shows that the detection of the target template via the MIP happens through the specific interaction of MIP cavities with the source antigen.

The amperometric assay is also performed to improve the speed of the biosensor's response to the viral template. In Figure 6c, a view of the amperometric response of the MIP at diverse concentrations of the viral template can be seen; the insert shows the respective calibration curve. Accordingly, the affinity of the reaction was amperometrically monitored through dropwise addition of the SARS-CoV-2 antigen to the electrolyte consisting of PBS with pH 7.4 at 0.05 V. Based on the obtained data, the concentration dependence of amperometric current for the MIP-based biosensor was found to be linear in the concentration range from 13.14 to 118.9 fg mL^{-1}. Moreover, the biosensors also demonstrated remarkable LOD and LOQ of about 11.32 and 12.01 fg mL^{-1}, respectively, toward detecting viral antigen, which is ideal for rapid and specific detection of SARS-CoV-2 antigen in biological media. Furthermore, the biosensor exhibited outstanding sensitivity of about 1.292 µA fg mL^{-1} cm^{-2}, which shows the incredible sensitivity of the MIP-based platform toward rapid and specific detection of the target antigen.

What is more, the applicability of the developed biosensor toward the detection of the viral template within actual biological samples was also assessed via DPV assay. The developed MIP-based biosensor is set on the optimized conditions, and

**ADVANCED
SCIENCE NEWS**

www.advancedsciencenews.com

**ADVANCED
MATERIALS
INTERFACES**

www.advmatinterfaces.de

Table 2. Determination of SARS-CoV-2 antigen in human plasma samples by the proposed method ($n = 5$).

Added Template [fg mL^{-1}]	Found Template [fg mL^{-1}]	%ER±RSD [%]
0	2.300	-
0.05	2.348	96.00±0.052
0.1	2.398	98.00±0.021
0.8	3.104	100.50±0.003
2	4.296	99.8±0.005
8	10.072	97.15±0.021

its analytical performance in actual plasma samples is examined via standard procedures. Correspondingly, the neat stock of SARS-CoV-2 antigen is five times diluted using 0.01 M PBS with pH 7.4 and then used to assess the performance of the molecularly imprinted polymer. For this aim, diverse concentrations of the viral antigen are spiked within the biological fluid, and their recovery rate is measured. The average recoveries were tabulated in **Table 2**, indicating the excellent performance of the as-developed biosensor toward accurate detection of SARS-CoV-2 in actual plasma samples with ideal selectivity, sensitivity, and specificity.

In addition, the sensor's selectivity was assessed by comparing the obtained responses via the electrochemical biosensor against the target template, i.e., SARS-CoV-2 antigen and interfering analytes at equivalent concentrations, i.e., 5 fg mL^{-1}. To evaluate the selectivity of the MIP-based biosensor, the effect of nine potential interferents, viz., H_1N_1 influenza virus with a concentration of $10^{7.3}$ TCID50, H_3N_2 influenza virus with a concentration of $10^{6.8}$ TCID50, glucose, lactose, maltose, ascorbic acid, sucrose, fructose, and bovine serum albumin, on the output response of the MIP-based biosensor, is assessed via the DPV assay. Correspondingly, the variation in the current response of the modified electrode to 5 fg mL^{-1} viral template in the presence of the interferences mentioned above was carefully assessed; a view of these outcomes can be seen in Figure 6d.

As depicted in Figure 6d, the developed MIP exhibited a superiorly high current response in interaction with the viral template, which shows the ideal selectivity and specificity of the as-prepared biosensor toward detecting SARS-CoV-2 antigens. On the other hand, the developed sensor did not show a noteworthy current response to the assessed analytes, which further highlights the biosensor's fantastic potential toward specific detection of target template even upon the presence of various kinds of potentially interfering compounds and viruses. More importantly, the MIP only showed high affinity toward the SARS-CoV-2 antigen and did not show noteworthy responses to other viruses such as H_1N1 and H_3N_2, indicating the specific/selective response of the as-developed MIP to the imprinted template.

The reproducibility of the MIP-based biosensor is also evaluated to check its stability toward detecting SARS-CoV-2 via DRP C110 screen printed electrodes. For this aim, the variation in the current response of five different independently fabricated MIP-based biosensors toward detecting the SARS-CoV-2 template with a concentration of 10 μg mL^{-1} is care-

fully assessed following standard procedures. The response peak intensity showed a relative standard deviation (RSD) of 4.98%, confirming that the obtained results are reproducible. Likewise, the fabrication repeatability of the biosensor is also examined via five independent measurements using an identical modified GCE with the MIP complex. The current response of five different electrodes was assessed, showing an RSD of about 4.22%, which lies in the satisfying range for a potential biosensor.

The stability of the SARS-CoV-2 MIP is also evaluated via standard protocols using DRP C110 screen printed electrodes. In this matter, the biosensor is stored at 4 °C for three days, and thence its current response is compared with the primary conditions. Achieved results exhibited a negligible decline in the current response of about 0.26 μA after three days. Furthermore, the sensor kept 93% of its performance after 21 days of storage at 4 °C. Obtained data from performed analyses confirmed the superior specificity, sensitivity, selectivity, and stability of the as-prepared biosensor toward detecting SARS-CoV-2 antigen in biological media, which is an excellent requirement for detecting fast transferable pathogenic viruses in actual aquatic samples.

3. Conclusions

The widespread of viral infectious diseases and their subsequent mortalities raised an urgent requirement for the design and fabrication of sensitive/specific diagnostic platforms capable of early detection of target viruses in the least time. For this regard, a highly specific artificial monoclonal antibody-based on a molecularly imprinted platform consisted of decorated GO with an interconnected complex of polypyrrole-boronic acid is developed. The as-developed MIP is accompanied by too many shape memory cavities that hold the information regarding the target template's size and chemical functional groups and act according to the "lock and key" mechanism, the same as a natural monoclonal antibody. The developed platform showed remarkable sensitivity, selectivity, stability, and specificity toward detecting the SARS-CoV-2 antigen in biological media. Correspondingly, the MIP configuration exhibited LOD of 0.326 and 11.32 fg mL^{-1} using voltammetric and amperometric assays, respectively, highlighting the superior capability and practicality of the prepared artificial antibody toward detection of SARS-CoV-2 antigen in actual biological specimens through a highly prompt manner.

Supporting Information

Supporting Information is available from the Wiley Online Library or from the author.

Acknowledgements

Conflict of Interest

The authors declare no conflict of interest.

Data Availability Statement

Research data are not shared.

Keywords

[1] Y. Saylan, Ö. Erdem, S. Ünal, A. Denizli, *Biosensors* **2019**, *9*, 65.

[2] a) J. Cui, F. Li, Z.-L. Shi, *Nat. Rev. Microbiol.* **2019**, *17*, 181; b) S. Su, G. Wong, W. Shi, J. Liu, A. C. Lai, J. Zhou, W. Liu, Y. Bi, G. F. Gao, *Trends Microbiol.* **2016**, *24*, 490; c) X. Zhu, X. Wang, L. Han, T. Chen, L. Wang, H. Li, S. Li, L. He, X. Fu, S. Chen, M. Xing, H. Chen, Y. Wang, *Biosens. Bioelectron.* **2020**, *166*, 112437; d) S. M. Mousavi, S. A. Hashemi, N. Parvin, A. Gholami, S. Ramakrishna, N. Omidifar, M. Moghadami, W.-H. Chiang, S. Mazraedoost, *Drug Metab. Rev.* **2021**, *53*, 141.

[3] A. Judd, J. Parry, M. Hickman, T. McDonald, L. Jordan, K. Lewis, M. Contreras, G. Dusheiko, G. Foster, N. Gill, *J. Med. Virol.* **2003**, *71*, 49.

[4] R. S. Lanciotti, A. J. Kerst, *J. Clin. Microbiol.* **2001**, *39*, 4506.

[5] J. Griffin, A. K. Singh, D. Senapati, E. Lee, K. Gaylor, J. Jones-Boone, P. C. Ray, *Small* **2009**, *5*, 839.

[6] S. Afsahi, M. B. Lerner, J. M. Goldstein, J. Lee, X. Tang, D. A. Bagarozzi Jr., D. Pan, L. Locascio, A. Walker, F. Barron, *Biosens. Bioelectron.* **2018**, *100*, 85.

[7] R. L. Caygill, G. E. Blair, P. A. Millner, *Anal. Chim. Acta* **2010**, *681*, 8.

[8] M. A. MacMullan, A. Ibrayeva, K. Trettner, L. Deming, S. Das, F. Tran, J. R. Moreno, J. G. Casian, P. Chellamuthu, J. Kraft, *Sci. Rep.* **2020**, *10*, 20818.

[9] a) A. Rump, R. Risti, M.-L. Kristal, J. Reut, V. Syritski, A. Lookene, S. R. Boudinot, *Biochem. Biophys. Res. Commun.* **2021**, *534*, 457; b) Y. Liu, Y. Liu, B. Diao, F. Ren, Y. Wang, J. Ding, Q. Huang, *MedRxiv* **2020**; c) M. L. Sin, K. E. Mach, P. K. Wong, J. C. Liao, *Expert Rev. Mol. Diagn.* **2014**, *14*, 225.

[10] a) S. A. Hashemi, S. Bahrani, S. M. Mousavi, N. Omidifar, M. Arjmand, N. G. G. Behbahan, S. Ramakrishna, K. B. Lankarani, M. Moghadami, M. Firoozsani, *Adv. Mater. Technol.* **2021**, 2100341; b) S. A. Hashemi, S. Bahrani, S. M. Mousavi, N. Omidifar, N. G. G. Behbahan, M. Arjmand, S. Ramakrishna, K. B. Lankarani, M. Moghadami, M. Shokripour, *J. Electroanal. Chem.* **2021**, *894*, 115341.

[11] S. A. Hashemi, N. G. G. Behbahan, S. Bahrani, S. M. Mousavi, A. Gholami, S. Ramakrishna, M. Firoozsani, M. Moghadami, K. B. Lankarani, N. Omidifar, *Biosens. Bioelectron.* **2021**, *171*, 112731.

[12] Y. Saylan, S. Akgönüllü, H. Yavuz, S. Ünal, A. Denizli, *Sensors* **2019**, *19*, 1279.

[13] L. Chen, S. Xu, J. Li, *Chem. Soc. Rev.* **2011**, *40*, 2922.

[14] S. A. Piletsky, N. W. Turner, P. Laitenberger, *Med. Eng. Phys.* **2006**, *28*, 971.

[15] J. Kupai, M. Razali, S. Buyuktiryaki, R. Kecili, G. Szekely, *Polym. Chem.* **2017**, *8*, 666.

[16] D. Liu, Q. Yang, S. Jin, Y. Song, J. Gao, Y. Wang, H. Mi, *Acta Biomater.* **2014**, *10*, 769.

[17] D. Cai, L. Ren, H. Zhao, C. Xu, L. Zhang, Y. Yu, H. Wang, Y. Lan, M. F. Roberts, J. H. Chuang, *Nat. Nanotechnol.* **2010**, *5*, 597.

[18] K. Rostamizadeh, M. Vahedpour, S. Bozorgi, *Int. J. Pharm.* **2012**, *424*, 67.

[19] D. Mathew, B. Thomas, K. Devaky, *React. Funct. Polym.* **2018**, *124*, 121.

[20] X. Yang, X. Dong, K. Zhang, F. Yang, Z. Guo, *J. Mater. Chem. B* **2016**, *4*, 920.

[21] A. Sarafraz-Yazdi, N. Razavi, *TrAC, Trends Anal. Chem.* **2015**, *73*, 81.

[22] S. Büyüktiryaki, R. Say, A. Denizli, A. Ersöz, *Talanta* **2017**, *167*, 172.

[23] Z. Iskierko, A. Checinska, P. S. Sharma, K. Golebiewska, K. Noworyta, P. Borowicz, K. Fronc, V. Bandi, F. D'Souza, W. Kutner, *J. Mater. Chem. C* **2017**, *5*, 969.

[24] E. Sari, R. Üzek, M. Duman, H. Y. Alagöz, A. Denizli, *Sens. Actuators, B* **2018**, *260*, 432.

[25] E. Sari, R. Üzek, M. Duman, A. Denizli, *J. Biomater. Sci., Polym. Ed.* **2018**, *29*, 1302.

[26] P. Wang, X. Sun, X. Su, T. Wang, *Analyst* **2016**, *141*, 3540.

[27] S. Ansari, *TrAC, Trends Anal. Chem.* **2017**, *90*, 89.

[28] S. Li, S. Cao, M. J. Whitcombe, S. A. Piletsky, *Prog. Polym. Sci.* **2014**, *39*, 145.

[29] Z. Altintas, M. Gittens, A. Guerreiro, K.-A. Thompson, J. Walker, S. Piletsky, I. E. Tothill, *Anal. Chem.* **2015**, *87*, 6801.

[30] C.-H. Lu, Y. Zhang, S.-F. Tang, Z.-B. Fang, H.-H. Yang, X. Chen, G.-N. Chen, *Biosens. Bioelectron.* **2012**, *31*, 439.

[31] I.-H. Baek, H.-S. Han, S. Baik, V. Helms, Y. Kim, *Polymers* **2018**, *10*, 974.

[32] C. J. Tan, Y. W. Tong, *Langmuir* **2007**, *23*, 2722.

[33] a) Z. Niu, M. A. Bruckman, B. Harp, C. M. Mello, Q. Wang, *Nano Res.* **2008**, *1*, 235; b) R. J. Tseng, C. Tsai, L. Ma, J. Ouyang, C. S. Ozkan, Y. Yang, *Nat. Nanotechnol.* **2006**, *1*, 72; c) A. Afzal, A. Mujahid, R. Schirhagl, S. Z. Bajwa, U. Latif, S. Feroz, *Chemosensors* **2017**, *5*, 7.

[34] D. Chen, H. Feng, J. Li, *Chem. Rev.* **2012**, *112*, 6027.

[35] P. T. Yin, S. Shah, M. Chhowalla, K.-B. Lee, *Chem. Rev.* **2015**, *115*, 2483.

[36] X. Zhao, P. Zhang, Y. Chen, Z. Su, G. Wei, *Nanoscale* **2015**, *7*, 5080.

[37] S. K. Krishnan, E. Singh, P. Singh, M. Meyyappan, H. S. Nalwa, *RSC Adv.* **2019**, *9*, 8778.

[38] W. Chee, H. Lim, N. Huang, I. Harrison, *RSC Adv.* **2015**, *5*, 68014.

[39] Z. Komeily-Nia, L.-T. Qu, J.-L. Li, *Small Sci.* **2021**, *1*, 2000026.

[40] a) S. M. Mousavi, F. W. Low, S. A. Hashemi, N. A. Samsudin, M. Shakeri, Y. Yusoff, M. Rahsepar, C. W. Lai, A. Babapoor, S. Soroshnia, *RSC Adv.* **2020**, *10*, 12851; b) R. Azhdari, S. M. Mousavi, S. A. Hashemi, S. Bahrani, S. Ramakrishna, *J. Environ. Chem. Eng.* **2019**, *7*, 103437.

[41] a) S. A. Hashemi, S. M. Mousavi, S. Bahrani, S. Ramakrishna, *J. Electroanal. Chem.* **2020**, *873*, 114406; b) S. A. Hashemi, S. M. Mousavi, S. Bahrani, S. Ramakrishna, A. Babapoor, W.-H. Chiang, *Anal. Chim. Acta* **2020**, *1107*, 183.

[42] a) L. Fritea, F. Bănică, T. O. Costea, L. Moldovan, C. Iovan, S. Cavalu, *J. Electroanal. Chem.* **2018**, *830*, 63; b) S. A. Hashemi, S. M. Mousavi, R. Faghihi, M. Arjmand, M. Rahsepar, S. Bahrani, S. Ramakrishna, C. W. Lai, *Polymers* **2020**, *12*, 1407; c) S. M. Mousavi, S. Soroshnia, S. A. Hashemi, A. Babapoor, Y. Ghasemi, A. Savardashtaki, A. M. Amani, *Drug Metab. Rev.* **2019**, *51*, 91.

[43] S. A. Hashemi, S. M. Mousavi, H. R. Naderi, S. Bahrani, M. Arjmand, A. Hagfeldt, W.-H. Chiang, S. Ramakrishna, *Chem. Eng. J.* **2021**, *418*, 129396.

[44] J. Luo, J. Huang, J. Cong, W. Wei, X. Liu, *ACS Appl. Mater. Interfaces* **2017**, *9*, 7735.

[45] H. Chen, M. Lee, J. Lee, J.-H. Kim, Y.-S. Gal, Y.-H. Hwang, W. G. An, K. Koh, *Sensors* **2007**, *7*, 1480.

[46] J. L. Urraca, M. C. Carbajo, M. J. Torralvo, J. González-Vázquez, G. Orellana, M. C. Moreno-Bondi, *Biosens. Bioelectron.* **2008**, *24*, 155.